Electromagnetic gyrokinetic turbulence in finite-beta helical plasmas[a)]

A. Ishizawa, T.-H. Watanabe, H. Sugama, S. Maeyama, and N. Nakajima

Citation: Physics of Plasmas (1994-present) **21**, 055905 (2014); doi: 10.1063/1.4876960
View online: http://dx.doi.org/10.1063/1.4876960
View Table of Contents: http://scitation.aip.org/content/aip/journal/pop/21/5?ver=pdfcov
Published by the AIP Publishing

Electromagnetic gyrokinetic turbulence in finite-beta helical plasmas[a)]

A. Ishizawa,[1,b)] T.-H. Watanabe,[1] H. Sugama,[1] S. Maeyama,[2] and N. Nakajima[1]
[1]National Institute for Fusion Science, Toki 509-5292, Japan
[2]Japan Atomic Energy Agency, Rokkasho, Aomori 039-3212, Japan

(Received 6 December 2013; accepted 17 February 2014; published online 14 May 2014)

A saturation mechanism for microturbulence in a regime of weak zonal flow generation is investigated by means of electromagnetic gyrokinetic simulations. The study identifies a new saturation process of the kinetic ballooning mode (KBM) turbulence originating from the spatial structure of the KBM instabilities in a finite-beta Large Helical Device (LHD) plasma. Specifically, the most unstable KBM in LHD has an inclined mode structure with respect to the mid-plane of a torus, i.e., it has a finite radial wave-number in flux tube coordinates, in contrast to KBMs in tokamaks as well as ion-temperature gradient modes in tokamaks and helical systems. The simulations reveal that the growth of KBMs in LHD is saturated by nonlinear interactions of oppositely inclined convection cells through mutual shearing as well as by the zonal flow. The saturation mechanism is quantitatively investigated by analysis of the nonlinear entropy transfer that shows not only the mutual shearing but also a self-interaction with an elongated mode structure along the magnetic field line. © *2014 AIP Publishing LLC*. [http://dx.doi.org/10.1063/1.4876960]

I. INTRODUCTION

Heliotron/stellarator devices confine plasmas with magnetic fields produced by external coils and thus are advantageous in maintaining a steady discharge.[1] The Large Helical Device (LHD) is a heliotron device and is free from current driven instabilities because of little net current. On the other hand, the pressure gradient driven instabilities, such as ballooning modes and interchange modes, may cause degradation of confinement in high-beta LHD experiments,[2–4] while drift-wave turbulence causes the anomalous transport in a low beta regime where the interplay between ion temperature gradient (ITG) turbulence and zonal flows has been investigated by means of electrostatic gyrokinetic simulations with adiabatic electrons.[5,6] Gyrokinetic simulation of electromagnetic turbulence in finite beta helical plasmas is an important task for predicting performance of helical fusion reactors and a great challenge in computational science due to complex three-dimensional magnetic structures as well as multiple spatio-temporal scales related to electromagnetic ion and electron dynamics.

Turbulent transport in finite-beta plasmas is studied by means of electromagnetic gyrokinetic simulations.[7–14] In finite-beta tokamak plasmas, the growth rate of ITG instability is suppressed by magnetic field line bending as plasma beta increases, while kinetic ballooning modes (KBMs) are destabilized at high beta. Whereas in low-beta torus plasmas, the zonal flow shear acts to regulate ITG driven turbulence, it has been observed by gyrokinetic simulations that instabilities continue to grow without reaching a physically relevant level of saturation at finite-beta tokamaks.[10,12] The corresponding problem in high-beta helical plasmas, the identification of a saturation mechanism for microturbulence in regimes where zonal flow generation is weak, is the subject of the present work. This problem has not been previously explored because of numerical difficulties associated with complex three-dimensional magnetic structures.

In this work, we investigate turbulent transport in finite-beta LHD plasmas by using GKV+ code solving the electromagnetic gyrokinetic equations.[13,14] The simulations reveal that the growth of KBM in LHD is saturated by nonlinear interactions of oppositely inclined convection cells through mutual shearing as well as by the zonal flow. The saturation mechanism is quantitatively investigated by analysis of the nonlinear entropy transfer.[15] The ratio of the turbulent energy flux to the potential fluctuation amplitude is smaller for the KBM turbulence at $\beta = 1.7\%$ than for the ITG turbulence at $\beta = 0.2\%$.

The paper is organized as follows. In Sec. II, our simulation models are described. In Sec. III, linear instabilities of standard LHD experiment with finite beta is studied by using a model configuration. In Sec. IV, KBM turbulence in the standard LHD is examined, and turbulent transport caused by them is presented. In Sec. V, the saturation mechanism of KBM turbulence is studied. Summary and discussion are given in Sec. VI.

II. SIMULATION MODEL

We consider a localized flux tube plasma along a magnetic field line. The distribution functions of gyro-centers are divided into the Maxwellian part and a perturbed part, $F_s = F_{Ms} + \delta f_s$, where $F_{Ms} = \frac{n_0}{(2\pi T_s/m_s)^{3/2}} \exp(-\frac{m_s v_\parallel^2}{2T_s} - \frac{\mu B}{T_s})$, and a perturbed part is represented by $\delta f_s = \sum_k \delta f_{sk} \exp(iS_k)$, where $\nabla S_k = \mathbf{k}_\perp$ and the subscript s denotes particle species. The model consists of the gyrokinetic equation of perturbed part of distribution functions,

[a)]Paper KI3 2, Bull. Am. Phys. Soc. **58**, 186 (2013).
[b)]Invited speaker.

$$\frac{D\delta f_{sk}}{Dt}+v_{\parallel}\mathbf{b}^{*}\cdot\nabla\delta f_{sk}=-i\mathbf{v}_{ds}\cdot\mathbf{k}_{\perp}\left(\delta f_{sk}+\frac{q_s}{T_s}F_{Ms}\phi_k J_{0s}\right)+v_{\parallel}\frac{q_s}{T_s}F_{Ms}E_{\parallel k}+\frac{\mu}{m_s}\mathbf{b}\cdot\nabla B\frac{\partial\delta f_{sk}}{\partial v_{\parallel}}+i\mathbf{v}_{*s}\cdot\mathbf{k}_{\perp}\frac{q_s}{T_s}F_{Ms}\left(\phi_k-\frac{v_{\parallel}}{c}A_{\parallel k}\right)J_{0s}+C_s, \tag{1}$$

the gyrokinetic Poisson and Ampere's equations,

$$k_{\perp}^2\phi_k=4\pi\sum_s q_s\left(\delta n_{sk}-\frac{q_s n_0}{T_s}(1-\Gamma_{0s})\phi_k\right), \tag{2}$$

$$k_{\perp}^2 A_{\parallel k}=\frac{4\pi}{c}\sum_s q_s n_0\delta u_{sk}, \tag{3}$$

where $E_{\parallel k}=-\mathbf{b}^{*}\cdot\nabla\phi_k J_{0s}-\frac{1}{c}\frac{\partial A_{\parallel k}J_{0s}}{\partial t}$, $\delta n_{sk}=\int\delta f_{sk}J_{0s}d^3v$, $n_0\delta u_{sk}=\int v_{\parallel}\delta f_{sk}J_{0s}d^3v$, $q_i=e$, $q_e=-e$. In Eq. (1), $\frac{Df_k}{Dt}=\frac{\partial f_k}{\partial t}+\frac{c}{B}[\phi J_{0s},f]_k$ and $\mathbf{b}^{*}\cdot\nabla f_k=\mathbf{b}\cdot\nabla f_k-\frac{1}{B}[A_{\parallel}J_{0s},f]_k$, where $[f,g]_k=-\sum_{k',k''}\delta_{k,k'+k''}\mathbf{b}\cdot\mathbf{k}'_{\perp}\times\mathbf{k}''_{\perp}f_{k'}g_{k''}$ and $J_{0s}=J_0(\rho_s k_{\perp})$, where J_0 is the zeroth order Bessel function. The drift velocities are $\mathbf{v}_{ds}=\frac{c}{q_sB}\mathbf{b}\times(\mu\nabla B+m_sv_{\parallel}^2\mathbf{b}\cdot\nabla\mathbf{b})$ and $\mathbf{v}_{*s}=\frac{cT_s}{q_sB}\mathbf{b}\times\nabla\ln F_{Ms}$, and

$$C_s=\nu_s\left[\frac{\partial}{\partial v_{\parallel}}\left(v_{\parallel}h_{sk}+v_{Ts}^2\frac{\partial h_{sk}}{\partial v_{\parallel}}\right)+\frac{1}{v_{\perp}}\frac{\partial}{\partial v_{\perp}}\left(v_{\perp}^2h_{sk}+v_{Ts}^2v_{\perp}\frac{\partial h_{sk}}{\partial v_{\perp}}\right)\right] \tag{4}$$

is the Lenard-Bernstein collision operator, where $h_{sk}=\delta f_{sk}+\frac{q_s}{T_s}\phi_k J_{0s}F_{Ms}$ is the non-adiabatic part of the perturbed part of gyro-center distribution function. In Eq. (2), $\Gamma_{0s}=e^{-\rho_s^2k_{\perp}^2}I_0(\rho_s^2k_{\perp}^2)$, where I_0 are the zeroth order modified Bessel function. Temperature and density gradients are uniform and are represented by the parameter $\eta_s=L_n/L_{Ts}$ in terms of density scale length $L_n=-(d\ln n/dx)^{-1}$ and temperature scale lengths $L_{Ts}=-(d\ln T_s/dx)^{-1}$.

The conservation equation of a quadratic quantity called entropy balance equation is obtained from Eqs. (1)–(3)[16] and is written as

$$\frac{d}{dt}\left(\sum_s\delta S_s+W_{es}+W_{em}\right)=\sum_s\left(\frac{\Theta_s}{L_{Ts}}+\frac{T_s\Gamma_s}{L_{ps}}+D_s\right), \tag{5}$$

where $\Theta_s=\sum_k\Theta_{s,k}$, $\Gamma_s=\sum_k\Gamma_{s,k}$, $\Theta_{s,k}=\Theta_{es,s,k}+\Theta_{em,s,k}$, $\Gamma_{s,k}=\Gamma_{es,s,k}+\Gamma_{em,s,k}$, $f=\sum_k f_k$, where

$$\delta S_{s,k}=\left\langle\int d^3v\frac{T_s|\delta f_{sk}|^2}{2F_{Ms}}\right\rangle, \tag{6}$$

$$D_{s,k}=\left\langle\int d^3v\frac{T_s}{F_{Ms}}\left(\delta f_{sk}^{*}+\frac{q_s}{T_s}\phi_k^{*}J_{0s}F_{Ms}\right)C_s\right\rangle, \tag{7}$$

$$W_{es,k}=\left\langle\left(\frac{k_{\perp}^2}{4\pi}+\sum_s\frac{n_0q_s^2}{T_s}[1-\Gamma_0(b_{sk})]\right)\frac{|\phi_k|^2}{2}\right\rangle, \tag{8}$$

$$W_{em,k}=\left\langle\frac{k_{\perp}^2}{4\pi}\frac{|A_{\parallel k}|^2}{2}\right\rangle, \tag{9}$$

$$\Theta_{es,s,k}=\left\langle Re\left[\left(\frac{1}{2}\delta p_{\parallel sk}+\delta p_{\perp sk}-\frac{5}{2}T_s\delta n_{sk}\right)\left(\frac{-ik_y\phi_kc}{B}\right)^{*}\right]\right\rangle, \tag{10}$$

$$\Theta_{em,s,k}=\left\langle Re\left[\left(\frac{1}{2}\delta q_{\parallel sk}+\delta q_{\perp sk}\right)\left(\frac{ik_yA_{\parallel k}}{B}\right)^{*}\right]\right\rangle, \tag{11}$$

$$\Gamma_{es,s,k}=\left\langle Re\left[\delta n_s\left(\frac{-ik_y\phi_kc}{B}\right)^{*}\right]\right\rangle, \tag{12}$$

$$\Gamma_{em,s,k}=\left\langle Re\left[n_0\delta u_s\left(\frac{ik_yA_{\parallel k}}{B}\right)^{*}\right]\right\rangle, \tag{13}$$

where $\langle\ \ \rangle$ and * denote the flux surface average and the complex conjugate, respectively, and $\delta p_{\parallel sk}=\int m_sv_{\parallel}^2\delta f_{sk}J_{0s}d^3v=n_0\delta T_{\parallel sk}+T_s\delta n_{sk}$, $\delta p_{\perp sk}=\int\mu B\delta f_{sk}J_{0s}d^3v=n_0\delta T_{\perp sk}+T_s\delta n_{sk}$, $n_0\delta q_{\parallel sk}=\int m_sv_{\parallel}^3\delta f_{sk}J_{0s}d^3v-3n_0T_s\delta u_{sk}$, $n_0\delta q_{\perp sk}=\int\mu Bv_{\parallel}\delta f_{sk}J_{0s}d^3v-n_0T_s\delta u_{sk}$ are parallel pressure, perpendicular pressure, parallel heat flux, and perpendicular heat flux, respectively.

The GKV+ code[13,14] is applied to the analysis of turbulent transport due to micro-instabilities at finite-beta in a model configuration of standard LHD plasmas. The magnetic field strength of the model LHD plasma is given by

$$B=B_0\left(1-\epsilon_{00}-\epsilon_t\cos z-\sum_{l=L-1}^{l=L+1}\epsilon_l\cos[(l-Mq_0)z-M\alpha]\right), \tag{14}$$

in terms of the flux tube coordinate $(x, y, z, v_{\parallel}, \mu)$,[17] where $L=2$, $M=10$, and $\alpha=0$, and the magnetic drift frequency is given by

$$\mathbf{v}_{ds}\cdot\mathbf{k}_{\perp}=\frac{-c}{q_s}\left(\mu+\frac{m_sv_{\parallel}^2}{B}\right)\frac{\epsilon_t}{r}\left[k_y\left(\frac{r\epsilon'_{00}}{\epsilon_t}+\frac{r\epsilon'_t}{\epsilon_t}\cos z+\sum_{l=L-1}^{l=L+1}\frac{r\epsilon'_l}{\epsilon_t}\cos[(l-Mq_0)z-M\alpha]\right)+(k_x+\hat{s}zk_y)\times\left(\sin z+\sum_{l=L-1}^{l=L+1}l\frac{\epsilon_l}{\epsilon_t}\sin[(l-Mq_0)z-M\alpha]\right)\right], \tag{15}$$

where $\hat{s}=(r/q)dq/dr$ and $\epsilon'=ad\epsilon/dr$.[5,18] Other parameters for the standard LHD configuration are $q_0=1.9$, $\hat{s}=-0.85$, $\eta_i=3$, $R/L_n=3.33$, $T_i=T_e$, $\epsilon_{00}=0$, $\epsilon_t=0.087$, and $(\epsilon_{L-1},\epsilon_L,\epsilon_{L+1})=\epsilon_t(-0.28,0.91,0)$. The normalizations used in our simulations are $(tv_{Ti}/L_n, \mathbf{k}_{\perp}\rho_i, v_{\parallel}/v_{Ts}, F_{Ms}v_{Ts}^3/n_0, \delta f_sL_nv_{Ts}^3/(\rho_in_0), \phi eL_n/(\rho_iT_i), A_{\parallel}L_n/(\rho_i^2B_0), m_s/m_i, T_s/T_i, n/n_0, B/B_0, q_s/e, \lambda_{Di}/\rho_i, \nu_sL_n/v_{Ts}) \rightarrow (t, \mathbf{k}_{\perp}, v_{\parallel}, F_{Ms}, \delta f_s, \phi, A_{\parallel}, m_s, T_s, n, B, q_s, \lambda_{Di}, \nu_s)$, where $\lambda_{Di}=\sqrt{T_i/(4\pi e^2n_0)}$ and $v_{Ts}=\sqrt{T_s/m_s}$, and the leading order of Larmor radius $\rho_{Ti}=v_{Ti}/\Omega_i$ is written as ρ_i. Ion and electron temperatures are

set to be equal $T_i=T_e$ in the following simulations, so that $\beta_i=\beta_e=\beta/2$, where $\beta_i=4\pi n_0 T_i/B_0^2$. In order to avoid electron temperature gradient instabilities at high wavenumber, the electron temperature gradient is set to be zero $\eta_e=0$ in our simulations. Turbulent transport due to the KBM at $\beta=1.7\%$ is investigated and is compared with the ITG turbulence at $\beta=0.2\%$. In the simulations, the number of Fourier modes is (144, ±36) with $(k_{x,min}\rho_i,\ k_{y,min}\rho_i)=(0.077,\ 0.058)$ for KBM and $(k_{x,min}\rho_i,\ k_{y,min}\rho_i)=(0.12,\ 0.046)$ for ITG, and 256, 64, and 32 grid points are distributed in the z, $v_{\|s}$, and μ direction. The resolution in the radial direction is required to capture an elongated mode structure along the magnetic field line by taking into account the magnetic shear that causes high-radial wavenumber Fourier modes. The resolution in the velocity space is required to reduce numerical error, so that numerical solutions satisfy the entropy balance equation. The electron-ion collision is neglected, and the collision frequency and the Debye length are set to be $\nu_i=2\times10^{-3}$, $\nu_e=2\times10^{-3}$, and $\lambda_{Di}/\rho_i=0$, respectively.

III. LINEAR ANALYSIS

Linear growth rates of instabilities in the model configuration of standard LHD are plotted in Fig. 1(a) as a function of k_y. The ITG mode is unstable for low β values 0.2% and 0.4%, and it has a peak of the growth rate around $k_y\rho_i=0.4$. The growth rate decreases with β. When the beta is larger than 1.2%, the KBM appears. The peak of the growth rate curve is located around $k_y\rho_i=0.18$. Figure 1(b) shows the radial mode number dependence of the growth rate of instability. The ITG mode is the most unstable at $k_x\rho_i=0$, while the KBM is the most unstable around $k_x\rho_i=0.3$, i.e., it has finite radial wavenumber in the flux tube coordinate. This is clearly shown by a color map of the linear growth rate of the KBM in the Fourier space $(k_x,\ k_y)$ in Fig. 1(c). This implies that the most unstable KBM in the LHD plasma has an inclined mode structure with respect to the mid-plane of a torus, while the ITG mode has horizontal mode structure. Figure 2 shows the mode structure of the ITG instability and the KBM on the $(x,\ y)$ plane at $z=0$. The inclined structure is clearly shown in the electrostatic potential profile. We remark that the inclined mode structure of the KBM is in contrast with that of KBMs in tokamaks.[13]

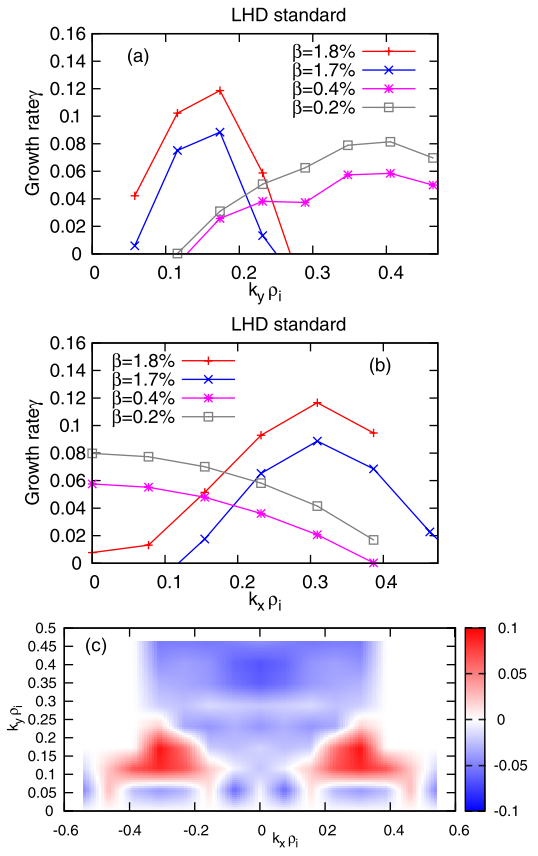

FIG. 1. Growth rates as functions of (a) $k_y\rho_i$ and of (b) $k_x\rho_i$ for the standard configuration of LHD with $\eta_e=0$, and (c) a color map of the linear growth rate of the KBM in the Fourier space $(k_x,\ k_y)$. The lines for $\beta=0.2\%$ and 0.4% ($\beta=1.7\%$ and $\beta=1.8\%$) show ITG modes (KBMs).

IV. TURBULENT TRANSPORT

Nonlinear simulations of the ITG turbulence with $\beta=0.2\%$ and of the KBM turbulence with $\beta=1.7\%$ in the

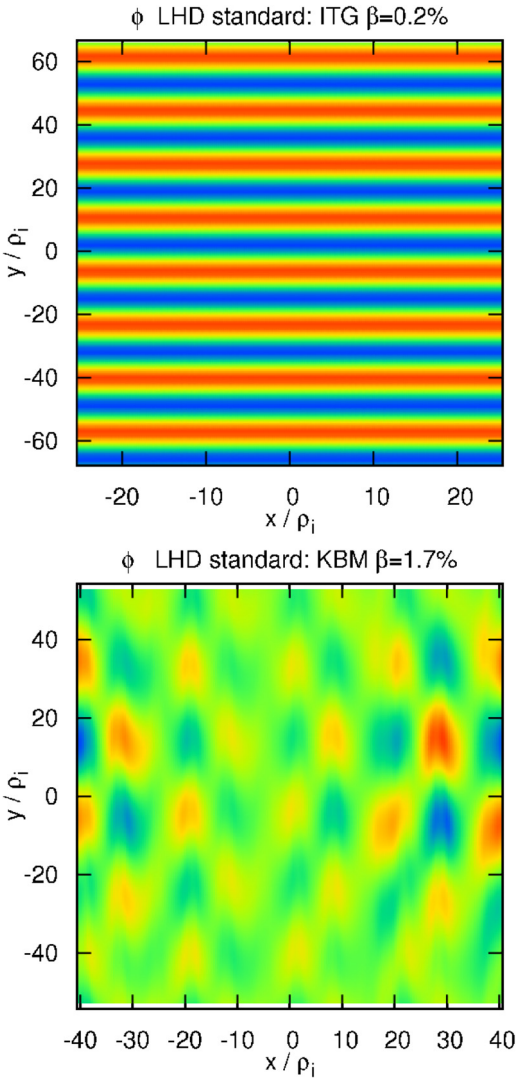

FIG. 2. Color map of electrostatic potential ϕ of ITG with $\beta=0.2\%$ and KBM with $\beta=1.7\%$ in the linear evolution on $z=0$. The unity of color is arbitrary.

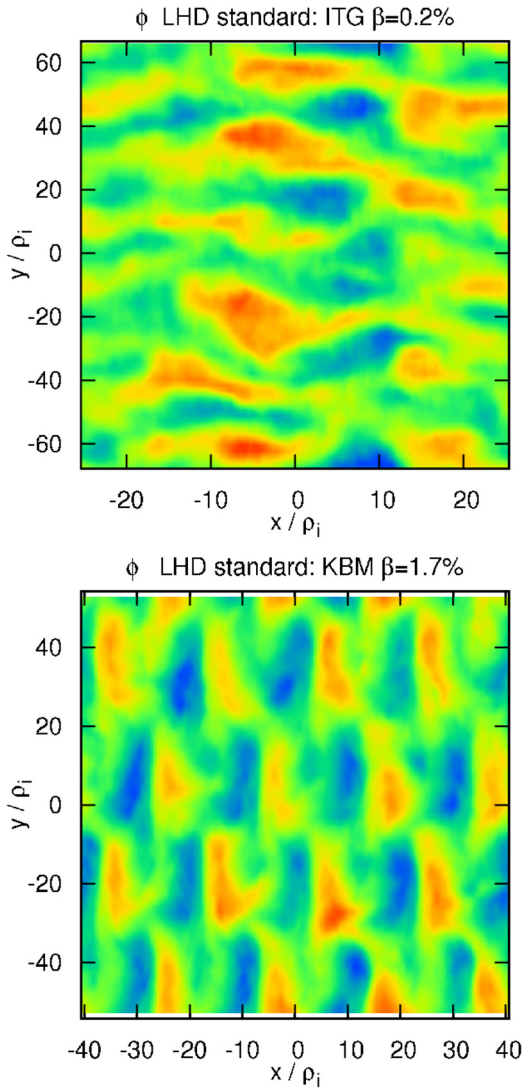

FIG. 3. Color map of ϕ in the steady state of the ITG turbulence with $\beta = 0.2\%$ and the KBM turbulence with $\beta = 1.7\%$ on $z = 0$.

model configuration of standard LHD are carried out. It is remarked that the growth rates of the most unstable KBM with $\beta = 1.7\%$ and of ITG instability with $\beta = 0.2\%$ are similar as shown in Fig. 1. Figure 3 shows color maps of electrostatic potential ϕ on $z = 0$. The potential profile shows that the zonal flow is regulating the ITG turbulence that extends to the longitudinal direction in the (x, y)-plane at $t = 180L_n/v_{Ti}$. On the other hand, the potential profile of the KBM at $t = 130$ is the superposition of the inclined stripes that are perturbed by small scale fluctuation. Figure 4 shows three-dimensional structure of the electrostatic potential in (x, y, z). The inclined stripes of the KBM turbulence are elongated along the magnetic field line z and have a peak at finite z. The peak is located around the minimum of magnetic drift frequency Eq. (15). On the other hand, the longitudinal stripes of ITG turbulence are not so elongated along the field line and are small at $z = \pm\pi/2$.

Figure 5 shows the time evolution of square of electrostatic potential for (a) the ITG mode with $\beta = 0.2\%$ and (b) the KBM with $\beta = 1.7\%$. In Fig. 5(a), the evolution of zonal flow potential $k_y = 0$, the most unstable ITG mode $k_y\rho_i = 0.37$ and a dominant ITG mode in the steady state $k_y\rho_i = 0.32$ are shown. At the beginning, the ITG mode with $k_y\rho_i = 0.37$ grows and produces zonal flows, and then it is saturated around $t = 70L_n/v_{Ti}$. The amplitude of the most unstable ITG mode with $k_y\rho_i = 0.37$ decreases after the growth of zonal flow, and the amplitudes of a dominant ITG mode with $k_y\rho_i = 0.32$ and of the zonal flow are comparable in a statistically steady state.

For the high-beta case $\beta = 1.7\%$, the KBM with $k_y\rho_i = 0.17$ grows exponentially at the beginning, then it is saturated around $t = 80L_n/v_{Ti}$ (Fig. 5(b)). Next, $k_y\rho_i = 0.12$ mode continues to grow and dominates, and then the system reaches a statistical steady state around $t = 130$. The amplitude of zonal flow potential $k = 0$ is an order of magnitude smaller than the dominant KBM with $k_y\rho_i = 0.12$ in the steady state. The weak zonal flow in the KBM turbulence is in contrast with the strong zonal flow in the ITG turbulence. Thus, the KBM turbulence is not regulated by zonal flows, in contrast to the ITG turbulence that is regulated by zonal flows.

The spectrum of the electrostatic potential $\langle|\phi_k|^2\rangle$ for the KBM turbulence with $\beta = 1.7\%$ and the ITG turbulence with $\beta = 0.2\%$ are plotted as a function of k_y in Fig. 6.

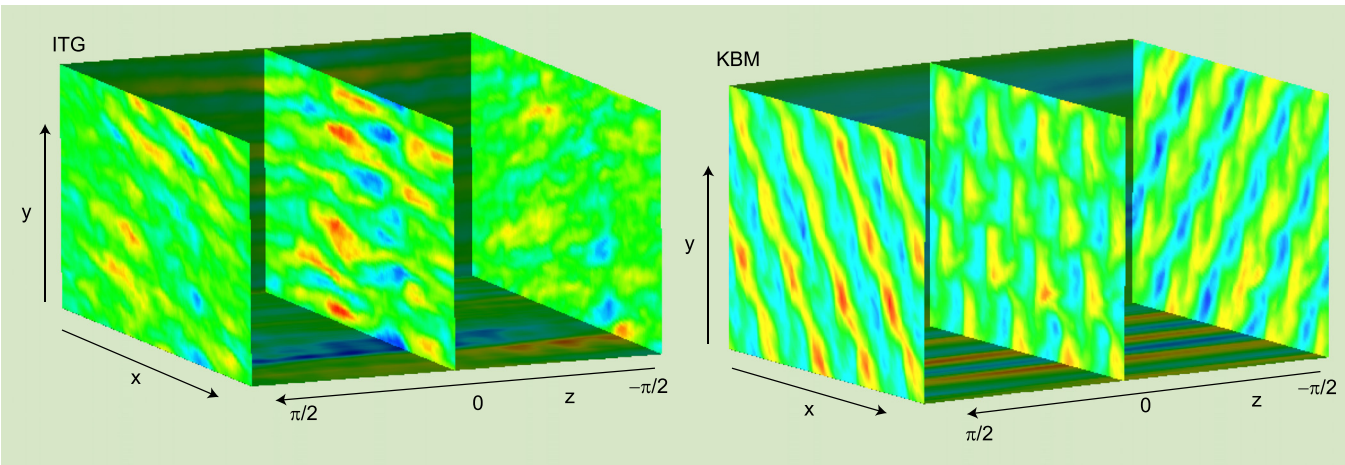

FIG. 4. Three-dimensional color map of ϕ in the steady state of the ITG turbulence with $\beta = 0.2\%$ and the KBM turbulence with $\beta = 1.7\%$.

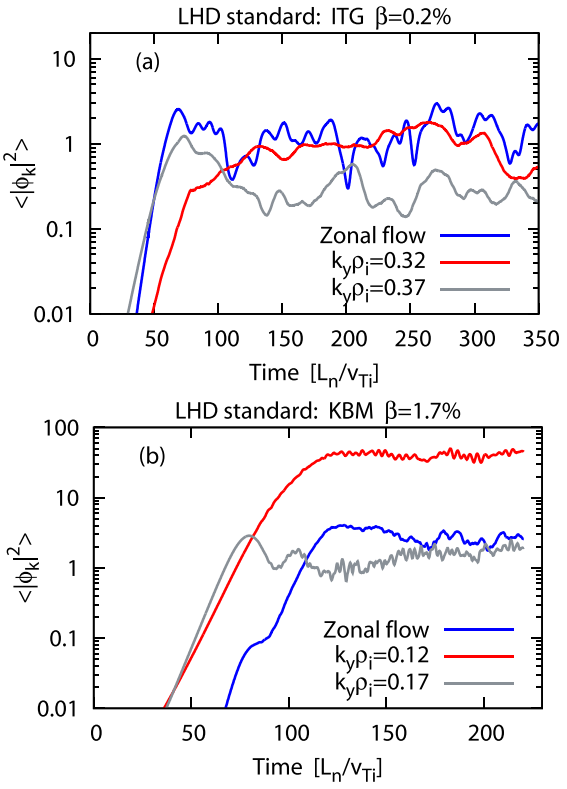

FIG. 5. Time evolution of square of electrostatic potential $\langle|\phi_k|^2\rangle$ of (a) ITG ((b) KBM) turbulence in the standard LHD for zonal potential $k_y=0$, the most unstable $k_y\rho_i=0.37$ ($k_y\rho_i=0.17$), and a dominant ITG (KBM) mode in the steady state of the standard LHD $k_y\rho_i=0.32$ ($k_y\rho_i=0.12$) with $\beta=0.2\%$ (1.7%).

The spectrum of KBM (ITG) turbulence is averaged from $t=150$ to 220 (from $t=120$ to 350). The spectrum of the KBM has a sharp peak at the dominant mode $k_y\rho_i=0.12$, and the zonal component $k_y=0$ and other modes are much smaller than the dominant mode. On the other hand, the spectrum of the ITG widely spreads in k_y compared with that of KBM, and the amplitude of the zonal component is comparable with those of the dominant ITG modes.

Figure 7 shows the time history of (a) the energy flux $Q_s=\Theta_s+\frac{5}{2}T_s\Gamma_s$ and (b) the particle flux Γ_s. For the ITG turbulence, the ion energy flux Q_{ion} becomes large as the ITG mode grows, and then it is in a steady state after $t=80L_n/v_{Ti}$ (Fig. 7(a)). The ion and electron particle fluxes,

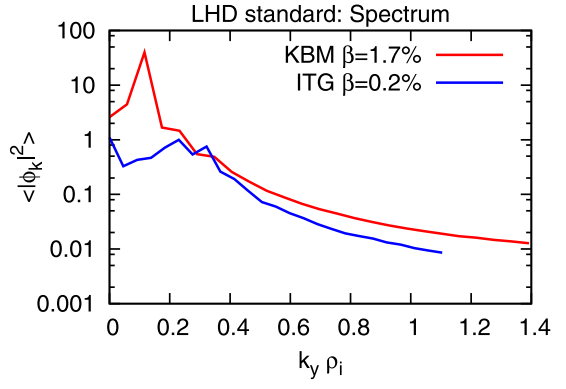

FIG. 6. Spectrum of electrostatic potential $\langle|\phi_k|^2\rangle$.

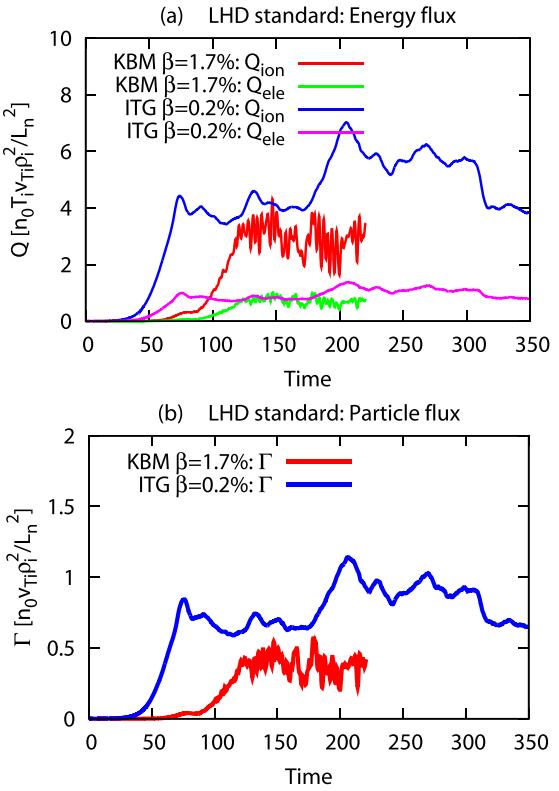

FIG. 7. Time history of (a) energy flux Q_s and (b) particle flux $\Gamma=\Gamma_{ion}=\Gamma_{ele}$ for the ITG with $\beta=0.2\%$ and the KBM with $\beta=1.7\%$.

Γ_{ion} and Γ_{ele}, are the same in Fig. 7(b), because of the Poisson equation and Ampere's law.[19] Table I summarizes the time averaged fluxes due to ITG turbulence, where the average is made from $tv_{Ti}/L_n=90$ to 450. The contribution of convective part $5\Gamma_{ion}/2$ to the energy flux Q_{ion} is comparable with that of the turbulent diffusion heat flux part Θ_{ion} for the ions. The transports due to the magnetic perturbation causing magnetic-flutter are much smaller than those by the electrostatic perturbation. In addition, the ion heat transport by the magnetic perturbation is small negative, and thus the magnetic perturbations of ITG turbulence have small pinch effects.[13]

TABLE I. Heat Θ_s $[T_iv_{Ti}\rho_i^2/L_n^2]$, particle $[\Gamma_s\,[n_0v_{Ti}\rho_i^2/L_n^2]$, and energy $Q_s=\Theta_s+\frac{5}{2}T_s\Gamma_s\,[n_0T_iv_{Ti}\rho_i^2/L_n^2]$ fluxes of the ITG turbulence at $\beta=0.2\%$ and of the KBM turbulence at $\beta=1.7\%$ in the model configuration of standard LHD plasma with $\eta_e=0$ by electrostatic perturbation, magnetic perturbation, and the sum of them.

ITG at $\beta=0.2\%$

	Θ_{ion}	Θ_{ele}	$\Gamma_{ion}=\Gamma_{ele}$	Q_{ion}	Q_{ele}
Electrostatic	2.94	−1.04	0.82	4.98	1.0
Magnetic	−0.01	0.01	−0.02	−0.05	−0.03
Total	2.93	−1.03	0.8	4.93	0.97

KBM at $\beta=1.7\%$

	Θ_{ion}	Θ_{ele}	$\Gamma_{ion}=\Gamma_{ele}$	Q_{ion}	Q_{ele}
Electrostatic	1.94	−0.45	0.37	2.86	0.47
Magnetic	−0.03	0.22	0.00	−0.02	0.23
Total	1.91	−0.23	0.37	2.84	0.70
Unit	$T_iv_{Ti}\rho_i^2/L_n^2$		$n_0v_{Ti}\rho_i^2/L_n^2$		$n_0T_iv_{Ti}\rho_i^2/L_n^2$

For the KBM turbulence in Fig. 7(a), the ion energy flux Q_{ion} starts to get saturated around $t=80$ with $Q_{ion} < 0.5T_i v_{Ti}\rho_i^2/L_n^2$ which is much smaller than the flux by ITG turbulence. This is related to the saturation of $k_y\rho_i=0.17$ mode in Fig. 5(b). Then, the flux Q_{ion} grows again because of the growth of $k_y\rho_i=0.12$ mode, and eventually the energy flux ($Q_{ion} \sim 3T_i v_{Ti}\rho_i^2/L_n^2$) becomes comparable to that due to the ITG turbulence. The electron energy flux Q_{ele} caused by the KBM is also comparable with that by the ITG turbulence in the steady state. The ion particle flux Γ_{ion} evolves in the similar way as the energy flux (Fig. 7(b)). It is saturated at a small level around $t=80$, then grows again and eventually reaches a steady state. The level of Γ_{ion} is similar to that of the ITG turbulence in the steady state. These fluxes caused by the KBM turbulence are summarized in Table I, where the average is made from $tv_{Ti}/L_n=120$ to 220. The ion energy and particle fluxes by the ITG turbulence with $\beta=0.2\%$ are larger than those by the KBM turbulence with $\beta=1.7\%$ (Fig. 7 and Table I), while the amplitude of the KBM turbulence is much larger than that of the ITG turbulence (Fig. 5). In addition, both of zonal flow amplitude and the transport are larger in the ITG turbulence than in the KBM turbulence.

Here, transfer of fluctuations caused by turbulence in the phase space is studied by means of the entropy balance equation (5). Figure 8 shows the time evolution of several groups of terms in the entropy balance equation (5): the sum of time derivative terms $d(\delta S_i+\delta S_e+W_{es}+W_{em})/dt$, the sum of transport terms $\Theta_s/L_{Ts}+\Gamma_s T_s/L_{ps}$, and the collisional dissipation term D_s, for (a) the ITG turbulence with $\beta=0.2\%$ and (b) the KBM turbulence with $\beta=1.7\%$. The time-derivative terms become small when a steady state is realized. In the steady state, the sum of ion heat and particle transport terms, $\Theta_i/L_{Ti}+\Gamma_i T_i/L_{pi}$, almost balances with the sum of ion and electron dissipation terms D_i+D_e for the ITG turbulence (Fig. 8(a)). The evolution of them for the KBM turbulence is similar to that for the ITG turbulence (Fig. 8(b)). The short period oscillations in the time derivative and the transport terms are caused by a nonlinearly excited linearly stable kinetic Alfvén wave.

V. SATURATION PROCESS OF KBM TURBULENCE

In Sec. V, the zonal flows in the KBM turbulence are weak. Here, we investigate the mechanism of the saturation of KBM through the nonlinear mode coupling in weak zonal flow by evaluating the nonlinear entropy transfer in the Fourier mode space.

The process of saturation of instabilities is studied by evaluating the entropy transfer function

$$T(\mathbf{k};\mathbf{k}',\mathbf{k}'') = \sum_s T_s(\mathbf{k};\mathbf{k}',\mathbf{k}''), \tag{16}$$

where

$$T_s(\mathbf{k};\mathbf{k}',\mathbf{k}'') = \mathrm{Re}\left\langle \int d^3v \frac{c}{B_0}\frac{T_s h_{sk}}{2F_{Ms}}\delta_{k,-k'-k''}\mathbf{b}\cdot\mathbf{k}'_\perp \times \mathbf{k}''_\perp(\chi_{sk'}h_{sk''} - h_{sk'}\chi_{sk''})\right\rangle, \tag{17}$$

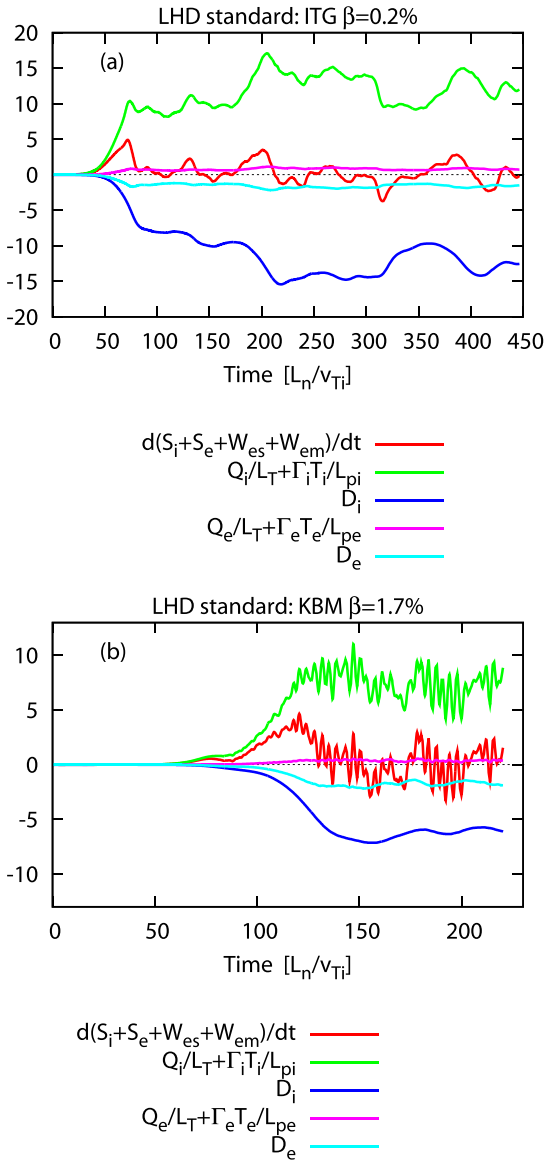

FIG. 8. Time evolution of each term in the entropy balance equation for (a) the ITG with $\beta=0.2\%$ and (b) the KBM with $\beta=1.7\%$.

where $h_{sk}=\delta f_{sk}+\frac{q_s}{T_s}\phi_k J_{0s}F_{Ms}$ is the non-adiabatic part of the perturbed part of gyro-center distribution function and $\chi_{sk}=(\phi_k - v_\parallel A_{\parallel k}/c)J_{0s}$ is the generalized potential. This is an extension to an electromagnetic version from the electrostatic one in Ref. 15. The transfer function satisfies the detailed balance equation, $T(\mathbf{k};\mathbf{k}',\mathbf{k}'')+T(\mathbf{k}';\mathbf{k}'',\mathbf{k}) +T(\mathbf{k}'';\mathbf{k},\mathbf{k}')=0$ and $T(\mathbf{k};\mathbf{k}',\mathbf{k}'')=T(\mathbf{k};\mathbf{k}'',\mathbf{k}')=T(-\mathbf{k};-\mathbf{k}',-\mathbf{k}'')$. The entropy balance equation for each Fourier mode is written by means of the transfer function as

$$\frac{d}{dt}\left(\sum_s \delta S_{s,k}+W_{es,k}+W_{em,k}\right) = \sum_s\left(T_{s,k}+\frac{\Theta_{s,k}}{L_{Ts}}+\frac{T_s\Gamma_{s,k}}{L_{ps}}+D_{s,k}\right), \tag{18}$$

where

$$T_{s,k}=\sum_{k',k''} T_s(\mathbf{k};\mathbf{k}',\mathbf{k}''). \tag{19}$$

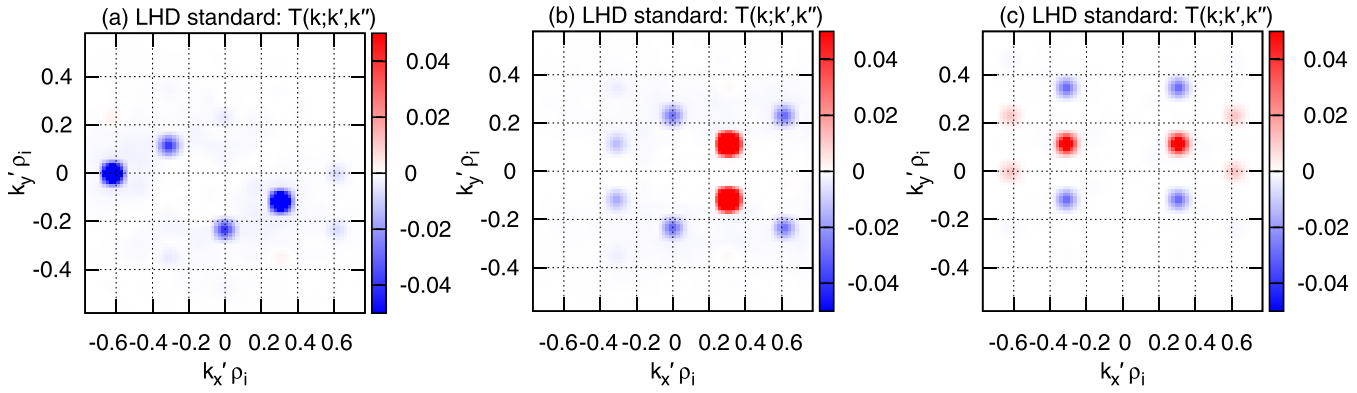

FIG. 9. Entropy transfer function $T(\mathbf{k};\mathbf{k}',\mathbf{k}'')$ averaged from $t=170$ to 180 for the KBM turbulence with $\beta=1.7\%$ in the standard LHD for (a) $(k_x\rho_i, k_y\rho_i)=(0.31, 0.12)$, (b) $(k_x\rho_i, k_y\rho_i)=(-0.62, 0)$, and (c) $(k_x\rho_i, k_y\rho_i)=(0, -0.23)$.

A. Mutual shearing by oppositely inclined convection cells

As we have seen in Fig. 5, the KBM with $(k_x\rho_i, k_y\rho_i)=(0.31, 0.12)$ dominates in the steady state around $t=170L_n/v_{Ti}$, we investigate the process of transfer of entropy/ free-energy from this mode around $t=170$. Figure 9 shows the entropy transfer function $T(\mathbf{k};\mathbf{k}',\mathbf{k}'')$ which is averaged from $t=150$ to 190. Figure 10 shows diagrams of entropy transfer caused by triad nonlinear mode interaction in the Fourier space. Figure 10(a) shows an element of the diagram, which is a triangle with the vertexes connected to three lines representing three energy transfer functions of the mode at the other end of the line, $T(\mathbf{k};\mathbf{k}',\mathbf{k}'')$, $T(\mathbf{k}';\mathbf{k}'',\mathbf{k})$, and $T(\mathbf{k}'';\mathbf{k},\mathbf{k}')$, where $T(\mathbf{k};\mathbf{k}',\mathbf{k}'')+T(\mathbf{k}';\mathbf{k}'',\mathbf{k})+T(\mathbf{k}'';\mathbf{k},\mathbf{k}')=0$. The arrows represent the signs of them, which are $T(\mathbf{k};\mathbf{k}',\mathbf{k}'')>0$, $T(\mathbf{k}';\mathbf{k}'',\mathbf{k})<0$, and $T(\mathbf{k}'';\mathbf{k},\mathbf{k}')<0$ in the figure as an example. Figure 10(b) shows the diagram of the entropy transfer for the KBM turbulence in the Fourier space. The blue arrows show the transfer of the entropy/free-energy from KBM to linearly stable modes through zonal flow shear, and the red arrows show the transfer through KBM/inclined-mode shear. It is remarked that a mode with (k_x, k_y) is the same as the complex conjugate of the mode with $(-k_x, -k_y)$. Figure 10(c) shows the diagram for the KBM turbulence. The black points represent the locations of Fourier

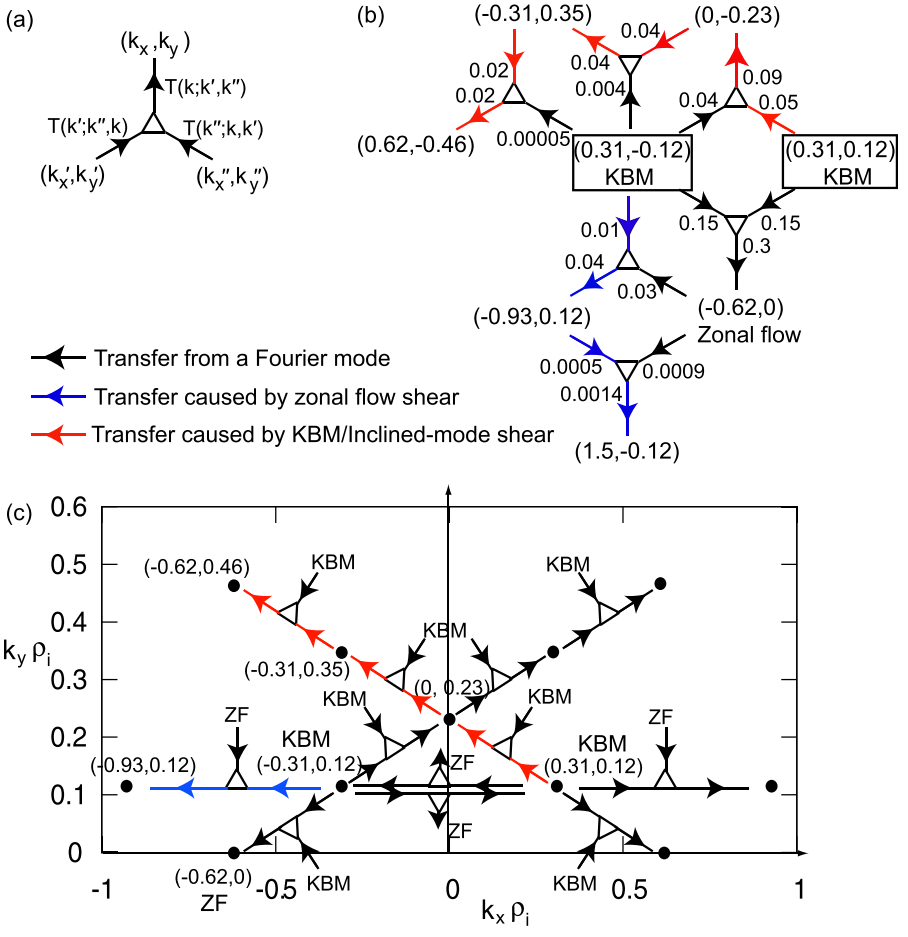

FIG. 10. Diagrams of nonlinear entropy transfer in the Fourier space: (a) an element of the diagram, which is a triangle with the vertexes connected to three lines representing three energy transfer functions of the mode at the other end of the line, $T(\mathbf{k};\mathbf{k}',\mathbf{k}'')$, $T(\mathbf{k}';\mathbf{k}'',\mathbf{k})$, and $T(\mathbf{k}'';\mathbf{k},\mathbf{k}')$, where $T(\mathbf{k};\mathbf{k}',\mathbf{k}'')+T(\mathbf{k}';\mathbf{k}'',\mathbf{k})+T(\mathbf{k}'';\mathbf{k},\mathbf{k}')=0$ and the arrows represent the signs of them, which are $T(\mathbf{k};\mathbf{k}',\mathbf{k}'')>0$, $T(\mathbf{k}';\mathbf{k}'',\mathbf{k})<0$ and $T(\mathbf{k}'';\mathbf{k},\mathbf{k}')<0$ in the figure as an example, (b) the diagram of the entropy transfer for the KBM turbulence in the Fourier space: blue arrows show the transfer of the entropy/free-energy from KBM to linearly stable modes through zonal flow shear and red arrows show the transfer through KBM/inclined-mode shear, (c) the diagram for the KBM turbulence where black points represent the locations of Fourier modes appearing in the diagram (b), and ZF → and KBM → show the scatter by the zonal flow shear and KBM/inclined-mode shear and are corresponding to arrows from zonal flow and KBM in (b).

modes appearing in the diagram in Fig. 10(b), and "ZF →" and "KBM →" show the scatter by the zonal flow shear and KBM/inclined-mode shear, respectively.

In Fig. 9(a), the map of $T(\mathbf{k};\mathbf{k}',\mathbf{k}'')$ for $\mathbf{k}=(k_x\rho_i,\ k_y\rho_i)=(0.31,\ 0.12)$ mode in $\mathbf{k}'$ space shows that there are strong negative points at $(k'_x\rho_i, k'_y\rho_i)=(0.31,-0.12)$ and $(-0.62,\ 0)$, and thus the $\mathbf{k}$ mode loses the entropy via nonlinear triad mode interactions with $(k'_x\rho_i, k'_y\rho_i)=(0.31,-0.12)$ and a zonal mode $(k''_x\rho_i, k''_y\rho_i)=(-0.62, 0)$. This transfer is indicated by the black arrow pointing to the left from the box of (0.31, 0.12) in Fig. 10(b) with the number of 0.15 showing the amount of the transfer. It is remarked $\mathbf{k}=-\mathbf{k}'-\mathbf{k}''$ and that the entropy transfer function is symmetric for $\mathbf{k}'$ and $\mathbf{k}''$. Next, the transfer functions of the zonal mode $(-0.62,\ 0)$ are examined. Figure 9(b) shows the transfer function for the zonal mode $(k_x\rho_i,\ k_y\rho_i)=(-0.62,\ 0)$. There are two large positive points at $(k'_x\rho_i, k'_y\rho_i)=(0.31, 0.12)$ and $(0.31,\ -0.12)$. Thus, the free-energy of the dominant KBMs $(k_x\rho_i,\ k_y\rho_i)=(0.31,\ 0.12)$ and $(0.31,\ -0.12)$ is transferred into the zonal mode $(k_x\rho_i,\ k_y\rho_i)=(-0.62,\ 0)$ resulting in the zonal flow component indicated by the black downward arrow between the boxes (0.31, 0.12) and (0.31, −0.12) with the amount of the transfer of 0.3 in Fig. 10(b). Although there is a strong transfer into the zonal component $(-0.62,\ 0)$, the zonal flow is very weak as shown in Figs. 5(b) and 6. Figure 9(a) also shows strong negative points at $(k'_x\rho_i, k'_y\rho_i)=(-0.31, 0.12)$ and $(0,\ -0.23)$, and thus the entropy is transferred into $(k'_x\rho_i, k'_y\rho_i)=(-0.31, 0.12)$ and $(k''_x\rho_i, k''_y\rho_i)=(0,-0.23)$. The transfer is indicated by the red leftward arrow from the box (0.31, 0.12) with the value of 0.05 in Fig. 10(a). Figure 9(c) shows the transfer function of $(k_x\rho_i,\ k_y\rho_i)=(0,\ 0.23)$. There are two large positive points at $(k'_x\rho_i, k'_y\rho_i)=(0.31, 0.12)$ and $(0.31,\ -0.12)$, and thus the entropy/free-energy of the dominant KBMs is also transferred into the $(0,\ -0.23)$ mode as shown by the red arrow towards $(0,\ -0.23)$ with the amount of the transfer 0.09. The transfer implies that oppositely inclined KBMs $(k_x\rho_i,\ k_y\rho_i)=(0.31,\ 0.12)$ and $(-0.31, 0.12)$ play an important role in their saturation.

Figure 10 summarizes the entropy transfer described in Fig. 9 and the transfer of other modes. There are two main directions of scatter of the entropy/free-energy from the dominant KBM to the high wavenumber region in the Fourier space $(k_x,\ k_y)$: one is the direction along the red arrows with "KBM/inclined-mode shear" and the other is the direction along the blue arrows with "zonal flow shear" in Fig. 10(b). The former is caused by a dominant KBM $(k_x\rho_i,\ k_y\rho_i)=(-0.31,\ 0.12)$ and is in the direction indicated by red arrows in Fig. 10(c). It causes the transfer in this inclined direction and subsequently transforms the entropy from the other dominant KBM $(k_x\rho_i,\ k_y\rho_i)=(0.31,\ 0.12)$ to $(0,\ -0.23)$ and then from $(0,\ -0.23)$ to $(-0.31,\ 0.35)$, and to higher Fourier modes, which are linearly stable as shown in the color map in Fig. 1(c). This subsequent scattering is interpreted as the shearing of KBM by the inclined mode. The inclined mode is also a dominant KBM, and thus the scatter in the inclined direction implies the saturation of KBMs by mutual shearing. The other main scatter is in the horizontal direction indicated by the blue arrows and is caused by the zonal component $(k_x\rho_i,\ k_y\rho_i)=(0.62,\ 0)$ in Fig. 10(c). The entropy/free-energy of the dominant KBM (−0.31,0.12) is transferred into (−0.93, 0.12) and then from (−0.93, 0.12) to (1.5, 0.12) as shown in Figs. 10(b) and 10(c). This scatter is caused by the zonal flow shear. The transfer by weak zonal flow might be related to that in Ref. 22 and would be studied in detail in our future work. The quantitative value of the transfer function of the triad mode interaction is described by the numbers along the red arrows in Fig. 10(b). It is remarked that the interaction between two dominant KBMs, (0.31, 0.12) and (−0.31, 0.12) includes the scatter by the zonal component; however, it is much smaller than the direct interaction between the KBMs. The amount of scatter by the zonal flow shear shown by a series of blue arrows with numbers 0.01, 0.04, 0.0005, and 0.00014 in Fig. 10(b) is smaller than that by the inclined KBM scatter shown by a series of red arrows with numbers 0.05, 0.09, 0.04, 0.04, 0.02, and 0.02 in Fig. 10(b). Hence, the growth of KBM is saturated by the nonlinear interactions of oppositely inclined convection cells through mutual shearing as well as the zonal flow. The color map of electrostatic potential in Fig. 3 shows the convection cells of the dominant KBMs.

B. Nonlinear interaction caused by an extended structure along the magnetic field line

In Subsection V A, it is shown that the saturation of KBM is caused by shearing between oppositely inclined convection cells and by zonal flow. In addition to this dominant mechanism, a saturation can be affected by nonlinear self-interaction due to an elongated mode structure along the magnetic field line.

In a flux tube model, we can describe a perturbation extending over $|\theta|=\pm\pi$ by connecting Fourier modes $(k_x,\ k_y)$ and $(k_x+2\pi\hat{s}k_y, k_y)$ through the boundary conditions by taking into account the magnetic shear, where $\hat{s}$ is the magnetic shear.[17] In this simulation $(k_x\rho_i,\ k_y\rho_i)=(0.31,\ 0.12)$ mode is connected to $(-0.31,\ 0.12)$ mode at $z=\pi$. When we solve a linearized equation in the flux tube geometry, the calculation of these connected modes gives exactly the same result as the calculation of $(k_x\rho_i,\ k_y\rho_i)=(0.31,\ 0.12)$ mode in the simulation box $-2\pi<z\le 2\pi$. However, in the nonlinear evolution, the $(-0.31,\ 0.12)$ mode can interact with the (0.31, 0.12) mode through nonlinear Fourier mode coupling. In fact, this interaction contributes the saturation of the growth of (0.31, 0.12) KBM. When the box size in the y-direction is doubled, the oppositely inclined KBM $(k_x\rho_i,\ k_y\rho_i)=(-0.31,\ 0.15)$ and the connected mode $(-0.46,\ 0.15)$ mode are different, and the transfer function of the dominant KBM (0.31, 0.15) shows that their contributions to the saturation are comparable (Fig. 11). Hence, the KBM is saturated not only by the shearing of oppositely inclined convection cells and zonal flow shear but also by the self-interaction due to the elongated mode structure along the magnetic field line in this simulation. The interaction caused by the elongated structure can be avoided by extending the simulation box along the field line, i.e., in z-direction, from $[-\pi:\pi]$ to $[-N_\theta\pi:N_\theta\pi]$ with an integer $N_\theta\ge 2$. The z-extended box may be more numerically efficient than a y-extended box. The extension of the simulation box may affect the saturation

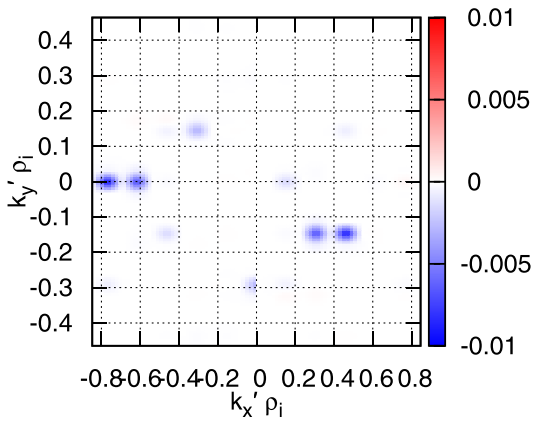

FIG. 11. Entropy transfer function $T(\mathbf{k};\mathbf{k}',\mathbf{k}'')$ of $(k_x\rho_i, k_y\rho_i) = (0.31, 0.15)$ for the KBM turbulence with doubled simulation box size in y-direction.

level of turbulence. Simulations with the extended box along the field line are retained in our future work.

VI. SUMMARY

Electromagnetic turbulence in finite-beta LHD plasmas is studied by means of gyrokinetic simulations. The study shows common features to those found in gyrokinetic simulations of finite beta tokamaks such as the stabilization of ITG modes, the destabilization of KBMs, and weak zonal flows in KBM turbulence.[13] The turbulent transport due to the ITG in LHD plasmas with $\beta = 0.2\%$ is regulated by zonal flows, even in the presence of electromagnetic perturbations. The contribution of convective part to the energy flux is comparable with that of the turbulent diffusive heat flux part, because of the finite density gradient of the model configuration of LHD. For a small density gradient that is often observed in LHD, the contribution of the convective part can be different from the results obtained here. In addition, magnetic perturbations have small pinch effects on the energy and the particle fluxes.

A new mechanism of saturation process of KBM turbulence in LHD is presented by analysis of nonlinear entropy transfer. The analysis has revealed that the growth of KBM is saturated by nonlinear interactions of oppositely inclined convection cells with mutual shearing as well as by the zonal flow. It is expected that the KBMs have inclined mode structure and are saturated through the new mechanism, when particle trapping by helical ripples is significant, because the bounce-average of magnetic drift velocity has finite radial component in the bounce-average of magnetic drift frequency Eq. (15) to destabilize Fourier modes with finite radial wavenumber. The new mechanism may also cause saturation of turbulence in finite-beta tokamaks in the presence of three-dimensionality such as toroidal ripples and resonant magnetic perturbation (RMP). In the steady state, the amplitudes of energy and particle fluxes due to KBM at $\beta = 1.7\%$ are similar to those caused by the ITG turbulence at $\beta = 0.2\%$, even though the amplitude of the KBM turbulence is larger than that of the ITG turbulence. The spectrum of electrostatic potential for the KBM turbulence is sharply peaked compared with that for the ITG turbulence.

It is found that a self-interaction produced by the elongated mode structure along the magnetic field line also plays a role in the process of saturation of KBM. The elongated structure is due to the electron dynamics along the field line, so it may appear in KBMs and ITG modes in general toroidal systems. The interaction can be avoided by extending the simulation box along the field line, i.e., in z-direction, from $[-\pi : \pi]$ to $[-N_\theta\pi : N_\theta\pi]$ with an integer N_θ or, for tokamaks, by using a new flux tube model.[20] The new flux tube model consists of a set of flux tubes aligned along the magnetic field line. The tubes are connected at their ends like cars in a train, so it will be referred as flux tube train model. Perturbations of turbulence in different tubes interact only through the boundary conditions, which take into account the magnetic shear, at the each end of the tubes. The model gives the same turbulent transport as the original one with increasing N_θ, and the new one is more efficient numerically, because it requires smaller radial resolution than the original one. It is remarked that the interaction due to the elongated mode structure is a dominant cause of a saturation of KBM in a tokamak when $N_\theta = 1$,[21] and that removing the interaction by extending the simulation domain in z-direction causes much higher level of turbulence. This will be reported in a separate paper.

ACKNOWLEDGMENTS

The work was supported by the Japanese Ministry of Education, Culture, Sports, Science and Technology, Grant Nos. 23561003 and 21560861 and by NIFS Collaborative Research Program (Nos. NIFS13KNTT020 and NIFS13KNST056). Authors would like to thank Professor R. Horiuchi for his support. The numerical simulations are carried out on the Plasma Simulator at National Institute for Fusion Science and the Helios Super Computer System at Computational Simulation Center of International Fusion Energy Research Center.

[1]O. Kaneko H. Yamada, S. Inagaki, and LHD Experiment Group, Nucl. Fusion **53**, 104015 (2013).
[2]K. Y. Watanabe, S. Masamune, Y. Takemura, H. Funaba, S. Sakakibara, and LHD Experiment Group, Phys. Plasmas **18**, 056119 (2011).
[3]S. Sakakibara, H. Yamada, K. Y. Watanabe, Y. Narushima, K. Toi, and LHD Experiment Group, AIP Conf. Proc. **669**, 203 (2003).
[4]S. Ohdachi, K. Tanaka, K. Y. Watanabe, and LHD Experiment Group, Contrib. Plasma Phys. **50**, 552 (2010).
[5]T.-H. Watanabe, H. Sugama, and S. F. Margalet, Phys. Rev. Lett. **100**, 195002 (2008).
[6]M. Nunami, T.-H. Watanabe, H. Sugama, and K. Tanaka, Phys. Plasmas **19**, 042504 (2012).
[7]J. Candy, Phys. Plasmas **12**, 072307 (2005).
[8]M. J. Pueschel, M. Kammerer, and F. Jenko, Phys. Plasmas **15**, 102310 (2008).
[9]M. J. Pueschel and F. Jenko, Phys. Plasmas **17**, 062307 (2010).
[10]R. E. Waltz, Phys. Plasmas **17**, 072501 (2010).
[11]D. R. Hatch, M. J. Pueschel, F. Jenko, W. M. Nevins, P. W. Terry, and H. Doerk, Phys. Rev. Lett. **108**, 235002 (2012).
[12]M. J. Pueschel, P. W. Terry, F. Jenko, D. R. Hatch, W. M. Nevins, T. Gorler, and D. Told, Phys. Rev. Lett. **110**, 155005 (2013).
[13]A. Ishizawa, S. Maeyama, T.-H. Watanabe, H. Sugama, and N. Nakajima, Nucl. Fusion **53**, 053007 (2013).
[14]S. Maeyama, A. Ishizawa, T.-H. Watanabe, N. Nakajima, S. Tsuji-Iio, and H. Tsutsui, Comput. Phys. Commun. **184**, 2462 (2013).

[15]M. Nakata, T.-H. Watanabe, and H. Sugama, Phys. Plasmas **19**, 022303 (2012).
[16]H. Sugama, T.-H. Watanabe, and M. Nunami, Phys. Plasmas **16**, 112503 (2009).
[17]M. A. Beer, S. C. Cowley, and G. W. Hammett, Phys. Plasmas **2**, 2687 (1995).
[18]S. Ferrando-Margalet, H. Sugama, and T.-H. Watanabe, Phys. Plasmas **14**, 122505 (2007).
[19]H. Sugama, M. Okamoto, W. Horton, and M. Wakatani, Phys. Plasmas **3**, 2379 (1996).
[20]T.-H. Watanabe, H. Sugama, A. Ishizawa, and M. Nunami, in *Bulletin of the American Physical Society, 53rd Annual Meeting of the APS DPP* (2013), Paper No. YP8.00065.
[21]S. Maeyama, A. Ishizawa, T.-H. Watanabe, M. Nakata, N. Miyato, M. Yagi, and Y. Idomura (unpublished).
[22]K. D. Makwana, P. W. Terry, and J.-H. Kim, Phys. Plasmas **19**, 062310 (2012).